

Stratospheric Ozone in the Last Glacial Maximum

Mingcheng Wang¹, Qiang Fu¹, Susan Solomon², Rachel H. White³ and Becky Alexander¹

¹Department of Atmospheric Sciences, University of Washington, Seattle, WA, USA

²Department of Earth, Atmospheric, and Planetary Sciences, Massachusetts Institute of
Technology, Boston, MA, USA

³Barcelona Supercomputing Center, Barcelona, Spain

Corresponding author: Mingcheng Wang (wmingch@uw.edu)

KEY POINTS

- Modeled ozone in Last Glacial Maximum compared to preindustrial increases in tropical lower stratosphere but decreases in most other regions
- Combined changes in stratospheric and tropospheric ozone lead to a decrease in total ozone column over the globe except in a few regions
- Surface ultraviolet radiation increases in the Northern Hemisphere extratropics, especially over the Laurentide ice caps, and near 60° S

ABSTRACT

Using the Whole Atmosphere Community Climate Model version 6, stratospheric ozone in the Last Glacial Maximum (LGM) is investigated. It is shown that, compared with preindustrial (PI) times, LGM modeled stratospheric temperatures increase by up to 8 K, leading to faster ozone destruction rates for gas phase reactions, especially via the Chapman mechanism. On the other hand, stratospheric hydroxyl radical (OH) and nitrogen oxides (NO_x) concentrations decrease by 10-20%, which decreases catalytic ozone destruction, thereby decreasing ozone loss rates. The net effect of these two compensating mechanisms in the upper stratosphere (above 15 hPa) is a vertically-integrated 1-3 Dobson Unit (DU) decrease during the LGM. In the lower stratosphere (tropopause to 15 hPa), changes in the stratospheric overturning circulation and resulting transport dominate changes in ozone. Consistent with a weakening of the residual circulation in the LGM, lower stratospheric ozone increases by 2-5 DU in the tropics and decreases by 5-10 DU in the extratropics, but the latter is partly compensated by ozone increases due to a lower tropopause. It is found that tropospheric ozone decreases by about 5 DU in the LGM versus PI. Combined changes in stratospheric and tropospheric ozone lead to a decrease in total ozone column everywhere except over the northeast of North America, equatorial Indian and west Pacific Oceans, and East Antarctica. Surface ultraviolet radiation in the LGM versus PI increases over the Northern Hemisphere mid- and high-latitudes, especially over the ice caps, and over the Southern Hemisphere near 60° S.

Key words: Stratospheric ozone, Last Glacial Maximum, ultraviolet radiation, WACCM6

1. Introduction

As a key component of the Earth system, stratospheric ozone protects life on Earth from hazardous ultraviolet (UV) radiation, and largely drives tropospheric chemistry. Rohrer and Berresheim [2006] showed that tropospheric hydroxyl radical (OH) is linearly correlated with UV radiation based on 5 years of measurements in Germany. Murray et al. [2014] found that stratospheric ozone, via its impact on surface UV radiation, is an important factor controlling variability in tropospheric OH over glacial-interglacial periods in a chemistry-climate model. In addition, stratospheric ozone could impact tropospheric climate [e.g. Nowack et al. 2015; Chiodo and Polvani, 2017; Noda et al., 2017; Szopa et al., 2019]. Szopa et al. [2019] found that modeled global surface temperature in the Eocene differed by as much as 14%, depending on whether the stratospheric ozone column abundance was consistently calculated or prescribed at preindustrial levels.

During the LGM, the stratosphere, including stratospheric ozone, is expected to be different from the preindustrial climate because of lower greenhouse gas concentrations (e.g., CO₂, CH₄, N₂O), wide-spread ice sheets (up to 3-4km thick) in the northern hemisphere (NH) and lower sea surface temperatures (SSTs). Compared to the rich literature on stratospheric ozone for the current and future climates, there are only a few studies on stratospheric ozone in the Last Glacial Maximum (LGM) [Crutzen and Brühl, 1993; Martinerie et al., 1995; Rind et al., 2009]. From a lack of better knowledge, past model simulations of the glacial climate have often assumed that stratospheric ozone is similar to the preindustrial climate [e.g., Valdes et al., 2005; Kaplan et al., 2006; Levine et al., 2011]. However, as indicated above, there are multiple reasons to expect ozone in the LGM to be different to the preindustrial distribution, and this study provides an analysis of these differences using a state-of-the-art chemistry climate model.

Pioneering research about stratospheric ozone in the LGM was carried out by Crutzen and Brühl [1993], who used a “one and a half” dimensional ($1^{1/2}$ -D) model. Martinerie et al. [1995] utilized a two-dimensional (2-D) model to further investigate the chemical composition of the atmosphere during the LGM. Both of these studies found only small changes in stratospheric ozone between the LGM and the preindustrial climate, despite large changes in atmospheric greenhouse concentrations. Rind et al. [2009] examined stratospheric ozone in the LGM using the 3-D GISS Global Climate Middle Atmosphere model ($4^\circ \times 5^\circ$ and 53 layers) with linearized ozone chemistry [McLinden et al. 2000]. The model used in Rind et al. [2009] did not consider stratospheric heterogeneous chemical processes nor tropospheric chemistry, but instead simulated tropospheric ozone using a simple relaxation approach. Rind et al. [2009] found that reduced nitrogen oxides (NO_x) and chlorine in the LGM lead to increases in stratospheric ozone, and much higher ozone concentrations in the polar, lower stratosphere associated with an intensified Brewer-Dobson Circulation (BDC) in the lowermost stratosphere, which in turn leads to stronger stratosphere-to-troposphere transport of ozone.

Recent ice core observations of a proxy for tropospheric oxidants suggested that tropospheric ozone concentrations may have been higher in cold climates compared to warm climates [Geng et al., 2017], the opposite of expectations based on changes in temperature-dependent surface emissions of ozone precursor gases. Geng et al. [2017] hypothesized that higher tropospheric ozone in the extratropics could be due to increased transport of stratospheric ozone to the surface driven by an enhanced BDC in the glacial climate [Rind et al., 2001; Rind et al., 2009]. An alternative hypothesis was that reactive halogen chemistry could be enhanced in the glacial climate, with potential implications for tropospheric ozone abundances [Geng et al., 2017]. Using the Whole Atmosphere Community Climate Model version 6 (WACCM6), Fu et al. [2020]

showed that the BDC during the LGM is consistently slower than modern climate. By transporting stratospheric ozone from the tropics, where it is produced, to the poles, the BDC plays a substantial role in determining the spatial distribution of ozone and thus surface UV radiation. This study analyzes the changes in ozone and UV radiation in the LGM including those resulting from changes in BDC, as simulated by WACCM6 [Fu et al., 2020].

This paper consists of four sections. Section 2 provides a brief description of WACCM6 and the model simulations. Section 3 presents the main results, and section 4 summarizes and concludes the paper.

2. Model Description and Simulations

2.1 Model description

The WACCM6 is the high-top atmospheric component of the NCAR Community Earth System Model 2 [Gettelman et al. 2019]; our simulations have a horizontal resolution of 0.9° latitude by 1.25° longitude with 70 vertical levels extending from the surface to 6×10^{-6} hPa (~ 140 km). In WACCM6, stratospheric heterogeneous chemical processes are parameterized following Wegner et al. [2013] and Solomon et al. [2015]. Chemical kinetics and photochemical rate constants have been updated following JPL 2015 recommendations [Burkholder et al., 2015]. The updated tropospheric chemistry scheme in WACCM6 leads to an improvement to the isoprene oxidation as well as other ozone precursors, and thus the tropospheric ozone simulation, as compared to the observations [Emmons et al., 2020]. WACCM6 was run by specifying SST and sea ice. We coupled the WACCM6 model with the CLM4.0 land model [Oleson et al., 2010], and utilized the CLM4.0 LGM lower boundary conditions from the CESM Paleo Working group [e.g., Brady et al., 2013]. In the LGM simulations, the plant functional type distribution is fixed under

preindustrial conditions but the leaf area index, vegetation height, and biogenic emissions are estimated as a function of the changed climate [Thornton et al., 2007; Guenther et al., 2012].

WACCM6 is able to reproduce variability in the middle atmosphere as derived from reanalyses (e.g., MERRA, ERA-Interim), including the frequency of Stratospheric Sudden Warmings [Gettelman et al., 2019] and BDC [Fu et al., 2020]. WACCM6 has an internally generated Quasi-Biennial Oscillation in the lower stratosphere [Garcia and Richter, 2019]. The WACCM model suite has a realistic evolution of the Southern Hemisphere (SH) springtime ozone hole over the latter half of the 20th century [Solomon et al., 2015]. For more details, the readers are referred to Gettelman et al. [2019].

2.2 Model simulations

Table 1 describes the simulations carried out explicitly for the study: 1) LGM simulation with prescribed SSTs derived from models (LGM_{PMIP3}), 2) LGM simulation with SSTs based on proxy data (LGM_{PROXY}), 3) preindustrial climate simulation (PI). With the first 10 years discarded for spin-up, the results presented here are based on the simulations from years 11 to 20; sensitivity studies extending simulations to 60 years find that using years 11-20 provides robust results for the analysis presented here.

The concentrations of CO₂, CH₄, and N₂O for the LGM (PI) are 185 (284) ppm, 349 (810) ppb and 200 (273) ppb, respectively. The surface concentrations of long-lived atmospheric species represent the year 1850 for the PI, and all anthropogenic emissions are turned off in the LGM. The orbital parameters are conditions 21,000 years ago for LGM simulations and year 1850 for the PI simulation. For the PI simulation, the SSTs/sea ice are the climatological averages of the year 1870-1890 based on observations [Rayner et al., 2003] and include a seasonal cycle. For LGM_{PMIP3},

we used the PMIP3 multi-model mean SST/sea ice for 7 models that had both LGM and historical runs [Braconnot et al., 2012]. The SSTs and sea ice for the LGM were then obtained as the model differences between the LGM and modern climate simulations plus corresponding observed SSTs/sea ice in modern climate [Fu et al., 2020]. For LGM_{PROXY}, the LGM-PI SST differences are taken from the MARGO proxy data [Kucera et al., 2005], while sea ice is the same as in LGM_{PMIP3}. The LGM ice sheet topography was from Abe-Ouchi et al. [2015].

For ozone-depleting substances, WACCM6 considers 17 organic halogens, among which four (i.e., methyl bromide, methyl chloride, dibromomethane and bromoform) include natural sources. Therefore, we set methyl bromide, methyl chloride, dibromomethane and bromoform surface mixing ratios in the LGM to preindustrial levels, and while the remaining 13 species are not included in the LGM and PI simulations. Emissions of CO and NO_x in the LGM were scaled with preindustrial emissions (Table 1) following Murray et al. [2014]. The CO emissions from fires, ocean and fuel combustion in the LGM were scaled to 0.1, 1 and 0 of the preindustrial levels while the NO_x emissions from fires, soil and fuel combustion in the LGM were scaled to 0.1, 0.98 and 0 of the preindustrial values. The emission of NO_x from lightning is simulated with the parameterization of Price and Rind [1992].

3. Results

3.1 Temperature changes

Figure 1 shows the annual- and zonal-mean temperature change for LGM_{PMIP3} versus PI. Herein the difference between LGM and PI is referred to as the ice-age effect. Due to the ice-age effect, the upper stratosphere in the LGM warms by up to 8 K, mainly because of much lower greenhouse gas concentrations and hence reduced radiative cooling to space. Such temperature

changes are consistent with previous studies [Rind et al., 2001; Rind et al., 2009], and have a significant impact on stratospheric ozone concentration in the LGM, as will be shown later. The temperature changes in the troposphere are largely a response to the changes of SST and greenhouse gases, showing a maximum cooling of more than 4 K in the tropical upper troposphere as well as a cooling of up to 6 K in the NH high-latitudes. Enhanced cooling is also seen over Antarctica. The global-mean surface air temperature is 10.0 °C in LGM_{PMIP3} and 10.5 °C in LGM_{PROXY}, close to the “warm” LGM (10.7 °C) of Murray et al. [2014] which was based on the SST reconstruction from CLIMAP [CLIMAP, 1976]. The result of LGM_{PROXY} is quite similar to LGM_{PMIP3} and thus not shown here.

3.2 Water vapor and hydroxyl radical (OH) changes

Water vapor transported from the tropical troposphere and oxidation of CH₄ in the stratosphere are the two primary sources of water vapor in the stratosphere [e.g., LeTexier et al., 1988]. Water vapor transported upward across the tropical tropopause is largely determined by tropical cold point tropopause (CPT) temperatures [e.g., Randel et al., 2004]. Figure 2 shows the annual- and zonal-mean CPT temperature and the water vapor concentration at the CPT versus latitude from the 3 simulations (left panels) and the changes relative to the PI (right panels). As compared to the PI, the ice-age conditions induce a cooling of ~1.5 K in the CPT in the tropics and NH high-latitudes, and 2-4 K cooling at the SH high-latitudes (Fig. 2b). It is also interesting to notice decreased cooling between about 35-65° latitudes in both hemispheres, which may be due to the equatorward shift of subtropical jets in cold climate [Fu et al., 2006; Fu and Lin, 2011]. Relative to PI, the water vapor concentration at the CPT in the LGM is decreased by ~1 ppmv in the tropics and up to 6 ppmv at high latitudes (Fig. 2d).

The relative changes of stratospheric water vapor, OH and NO_x for LGM_{PMIP3} versus PI are shown in Fig. 3, in which the climatology of PI is superimposed as contours in ppmv, pptv, and ppbv, respectively. Stratospheric water vapor tends to increase with height because of increasing CH₄ oxidation [LeTexier et al., 1988]. There is a local minimum of water vapor concentration at the south pole owing to extreme cold temperatures there and associated dehydration through cloud particle sedimentation. Relative to PI, stratospheric water vapor in the LGM decreases everywhere, with a 10-25% decrease in the lower and middle stratosphere and a ~20% decrease in the upper stratosphere, as a consequence of much lower atmospheric CH₄ concentrations (Table 1), and the colder tropical CPT (Fig. 2b) leading to less water vapor transported from the troposphere (Fig. 2d). OH is mainly produced by the reaction of excited atomic oxygen, O(¹D), with water vapor. In line with the decrease in stratospheric water vapor, the stratospheric OH decreases by 10-20% over the bulk of the stratosphere during the LGM. The detailed pattern of OH changes (Fig.3b) is determined by the changes of both H₂O (Fig. 3a) and O(¹D), and the latter is governed largely by the change in UV radiation. The reaction of N₂O with O(¹D) is the major source of stratospheric NO_x. Because of much higher UV radiation at higher altitudes, the climatological NO_x concentrations tend to increase with height, maximizing around 2 hPa (Fig. 3c). Due to the much lower N₂O concentration in the LGM, the NO_x mixing ratio decreases by 10-20% in the stratosphere, with small increases around the south pole and 100 hPa. The detailed pattern of NO_x changes (Fig.3c) is again determined by the changes of both N₂O and O(¹D), and the small increases of NO_x concentrations around the south pole and 100 hPa may be due to increases of O(¹D) in those regions (not shown).

Compared with LGM_{PMIP3}, more water vapor is transported from the troposphere into the stratosphere in LGM_{PROXY} because of the warmer tropical SST. Both stratospheric water vapor and

OH in LGM_{PROXY} are thus a bit higher than LGM_{PMIP3}, but the changes relative to PI remain similar (not shown). For brevity, unless otherwise indicated, the results of LGM_{PROXY} are not shown in the following discussions.

3.3 Ozone change

Figure 4 shows the ozone change for LGM_{PMIP3} versus PI. Relative to the PI, ice-age conditions lead to ozone decreases in most of the stratosphere, except for the tropical lower stratosphere where the ozone increases by 5-15%, extending up to about 20 hPa. The increase of ~5% near 10 hPa is caused by the maximum reductions in OH and NO_x there (Fig. 3) while the increase around 100 hPa over the SH high-latitudes is linked to the local intensification of BDC in the spring season [see Fig. 3e in Fu et al., 2020]. The increases near ~300 hPa in both NH and SH extratropics are caused by lower tropopauses in the LGM which will be discussed latter. The increase in tropical lower stratospheric ozone is due to a decrease in the BDC in the LGM [Fu et al., 2020] and will be further discussed later. Compared to PI, major catalysts of stratospheric ozone destruction including both OH and NO_x decrease in the LGM (Fig. 3), which will act to increase stratospheric ozone loss rates. On the other hand, owing to the reduced greenhouse gas concentrations, the stratosphere warms by up to 8 K in the LGM (Fig. 1). It is well known that stratospheric ozone in the upper stratosphere has an inverse relationship with temperature linked to gas-phase kinetic factors for several reactions displaying an energy of activation. For example, as shown in Jonsson et al. [2004], in response to doubled CO₂-induced stratospheric cooling, stratospheric ozone increases because of slowing of the Chapman reaction $O + O_3 \rightarrow 2O_2$ and thus slower ozone destruction rates. A warmer LGM stratosphere, on the other hand, leads to faster ozone loss reaction rates due to temperature-sensitive reactions which act to lower ozone

concentrations. The net result of these compensating effects is only a 5-10% decrease in upper stratospheric ozone despite large changes in stratospheric temperatures, generally consistent with previous LGM studies [Crutzen and Brühl, 1993; Martinerie et al., 1995].

Unlike the upper stratosphere, in which ozone photochemistry dominates, the BDC plays a significant role in determining the lower stratospheric ozone distribution. Following Li et al. [2009], the mean advective ozone transport $-(\overline{w^*} \frac{\partial \overline{O_3}}{\partial z} + \overline{v^*} \frac{\partial \overline{O_3}}{\partial y})$ in the model is presented in Fig. 5. Here, $\overline{w^*}$ and $\overline{v^*}$ are the transformed Eulerian mean (TEM) residual vertical and meridional velocity [Andrews et al., 1987], and $\overline{O_3}$ is the zonal mean ozone mixing ratio. The vertical $(-\overline{w^*} \frac{\partial \overline{O_3}}{\partial z})$ and meridional $(-\overline{v^*} \frac{\partial \overline{O_3}}{\partial y})$ components of advective ozone transport are also shown (middle and far-right panels of Fig. 5). In the lower stratosphere (below ~15 hPa), the advective ozone transport is negative in the tropics but positive in the extratropics. By contrast, there is positive (negative) advective ozone transport in the tropics (extratropics) in the upper stratosphere. Generally, the advective ozone transport pattern is dominated by the vertical component because of much larger ozone vertical gradients compared to those in the horizontal (see contours of Fig. 4). It is interesting to note that meridional ozone transport tends to increase ozone everywhere, except in the subtropical jet regions around the tropopause. The vertical and meridional advective ozone transport are stronger in the NH than the SH, reflecting the stronger BDC there [Rosenlof, 1995].

Fu et al. [2020] found that the BDC in the LGM is slower than that in the modern climate, regardless of SSTs prescribed. Consistent with the weakening BDC in the LGM, the change of advective ozone transport (Figs. 5d-5f) is similar to, but generally the reverse sign of, the climatological pattern (Figs. 5a-5c). The positive change of ozone advective transport in the tropical lower stratosphere (Fig. 5d) explains the increase of ozone there in the LGM as already noted above (Fig. 4). The ozone advective lifetime is comparable with the chemical loss lifetime

around 70 hPa but becomes much longer in the upper stratosphere [Li et al., 2009]. Hence, although LGM changes to advective ozone transport act to increase ozone in the upper stratosphere in the middle and high latitudes, chemical processes strongly dominate in this region, resulting in ozone decreases there.

In order to further quantify the changes of ozone in the LGM, the total ozone column is divided into three parts: the upper stratospheric column (above 15 hPa) where chemical processes dominate, the lower stratospheric column (below 15 hPa but above the tropopause) where dynamical transport dominates, and the tropospheric column (below the tropopause). Based on *in situ* trace gas measurements, Pan et al. [2018] illustrated that the World Meteorological Organization lapse rate tropopause (LRT) [World Meteorological Organization, 1957] did better than the CPT in identifying the transition from the tropopause to the stratosphere. Therefore, the partitioning between the stratospheric and tropospheric ozone column is based on LRT, namely the lower boundary of a layer in which the temperature lapse rate is less than 2 K km^{-1} for a depth of at least 2 km.

Figure 6 shows the annual- and zonal-mean latitudinal distributions of partial ozone columns (upper panels) and their changes relative to the PI (lower panels). Since the lifetime of ozone related to chemical processes is much shorter than the timescale of advective transport in the upper stratosphere and the rate of ozone production is larger when the solar angle is smaller [Brasseur and Solomon, 2006], the upper stratospheric ozone column peaks in the tropics and decreases toward the high latitudes (Fig. 6a). In contrast, the lower stratospheric ozone column (Fig. 6b) maximizes in the high latitudes, with a minimum at the tropics, mainly because of advective ozone transport. As expected, most of the ozone resides in the stratosphere, and tropospheric ozone (Fig. 6d) is only a small proportion ($\sim 10\%$) of the total ozone column, with

higher concentrations in mid-latitudes and higher concentrations in the NH than the SH. This results from higher photochemical ozone production related to higher natural continental emissions of CO, NO_x and hydrocarbons in the NH relative to the SH [e.g., Logan, 1985; Lelieveld and Dentener, 2000].

Due to the compensating effects of changes in major catalysts of ozone destruction (OH and NO_x) and temperature, ice-age conditions lead to a small (~1-3 DU) decrease of the upper stratospheric ozone column relative to PI (Fig. 6f). Because of the weakening BDC, the lower stratospheric ozone column increases by about 2-5 DU in the tropics and decreases by 5-10 DU in the extratropics (Fig. 6g). The modeled change in the total stratospheric ozone column (Fig. 6h) is dominated by change in the lower stratospheric ozone column (Fig. 6g). A reduced decrease (i.e., an increase) of lower-stratospheric ozone (Fig. 6g) in the NH (SH) high latitudes is partly because of a lower tropopause there in the LGM as shown later.

As compared with PI, the tropospheric ozone column decreases by ~ 5DU (30%) in the LGM (Fig. 6i), which is within the range reported by previous modeling studies (see Table 1 summarized by Murray et al. [2014]). The ice-age conditions lead to decreases (5-15 DU) of total ozone column at almost all latitudes (Fig. 6j). The latitudinal dependence of the total ozone column change is dominated by the lower stratospheric ozone column change (Fig. 6g) while the tropospheric change shifts the total change down by about 5 DU. Near the equator and south pole the stratospheric and tropospheric ozone column changes tend to cancel each other.

Figure 7 shows the spatial distribution of stratospheric ozone column in the PI and change for LGM versus PI. As compared with PI, stratospheric ozone increases slightly in the tropics but decreases by up to 25 DU in mid- and high latitudes. The larger decrease of the stratospheric ozone column in the NH relative to the SH is due to the larger magnitude decrease of the BDC in the NH

[Fu et al., 2020]. It is interesting to note that a significant increase (~ 25 DU) of the stratospheric ozone column is found in northeast North America, which is collocated with the maximum LRT pressure increase (Fig. 8) and a strong local intensification of downward vertical motion (not shown). Those changes are probably driven by the presence of the Laurentide ice sheet.

In order to quantify the relative contributions of changes in the height of the tropopause versus changes in transport on the lower stratospheric ozone column change in the LGM, we integrate the LGM stratospheric ozone field vertically but impose the PI tropopause. The stratospheric ozone column change arising from the tropopause change is approximated by the difference between the result using the LGM ozone field combined with the PI tropopause and the result using the LGM ozone and tropopause fields. By subtracting the contribution of tropopause change from the lower stratospheric ozone column change, the residual is referred to as the transport contribution. Figure 9 shows the spatial distributions of upper and lower stratospheric ozone column changes for LGM_{PMIP3} versus PI, and the contributions to the latter from the tropopause change and transport change. Consistent with Figure 6, the stratospheric ozone column change in the LGM (Fig. 7b) is dominated by the lower stratospheric ozone change (Fig. 9b). Further, we note that the contribution from tropopause changes leads to an increase of stratospheric ozone column in the extratropics (Fig. 9c), which can also be seen in Fig. 4 near 300 hPa. Although these changes are generally much smaller than those from transport changes (Fig. 9d), they do partly compensate for the ozone decreases due to the circulation changes in the extratropics, especially in the SH (Figs. 9 and 6).

Figure 10 is the same as Figure 7, but for the tropospheric ozone column. Relative to the PI, the tropospheric ozone column in the LGM is decreased (~ 5 DU) everywhere, maximized around North America, which may be due to the decrease of biogenic emissions and much higher

tropospheric photolysis (Figs. 13b) caused by the ice sheets. Here, the tropospheric ozone change for the LGM versus PI is consistent with theoretical expectation based on temperature-dependent surface emission of ozone precursor gases, and does not support the hypothesis of Geng et al. [2017] that the transport of stratospheric ozone to the surface, driven by a stronger BDC, increases in the glacial climate.

Figure 11 is the same as Figure 7, but for the total ozone column. Compared to PI, the total ozone column in the LGM is decreased almost everywhere, except at the Northeast of North America, equatorial Indian and west Pacific Oceans, and Antarctic between 60 and 150° E, because of larger stratospheric ozone increases (Fig. 7b) relative to the tropospheric ozone decreases (Fig. 10b) in those regions.

3.4 UV radiation change

Ozone is one of the major factors determining surface UV radiation [Lamy et al., 2019], which in turn drives photochemical reactions in the troposphere. In this subsection, we investigate the change of photolytic rate constant (J_{O1D}) of $O_3 + h\nu \rightarrow O_2 + O(^1D)$, which is driven by photons at wavelengths shorter than 320 nm. Figure 12 shows the annual- and zonal-mean J_{O1D} (day^{-1}) change for LGM versus PI. Because of the absorption of UV radiation by ozone, climatological J_{O1D} tends to decrease toward the surface, with the largest values in the tropics due to low ozone columns and small solar angles. Compared to the PI, J_{O1D} in the LGM decreases in the tropics and SH high latitudes, extending from 50 hPa toward the surface, but increases in other regions. The decreases of J_{O1D} for the LGM versus PI in the tropics and SH high latitudes are due to the increases of stratospheric ozone concentrations there (Fig. 4), and the increases in other regions are caused by the decreases in total ozone column abundance (Fig. 11b). It is also noted that there are

enhanced increases in J_{O1D} in the NH and SH mid-latitudes near ~ 700 hPa.

Figure 13 shows the changes in the spatiotemporal distribution of surface J_{O1D} in the LGM. The seasonal cycle of surface J_{O1D} follows the seasonal progression of the solar zenith angle (Fig. 13a). A maximum of surface J_{O1D} occurs over the Sahara Desert, which is related to the high surface albedo there. Higher J_{O1D} also occurs in regions with high topography, e.g. Tibet and Andes, because of higher elevations and thus smaller solar attenuation by the atmosphere. In line with the change of total ozone column (Fig. 11b), surface J_{O1D} in LGM decreases in the tropics and the Antarctic, but increases in most of other regions, with the largest increase in North America and Europe in the boreal summer season caused by the increase in surface albedo and smaller solar attenuation resulting from the large ice sheets there. A large increase of surface J_{O1D} is also found over the SH near 60° S, which is due to increased sea ice extent in the LGM. The relative change of surface J_{O1D} for LGM versus PI is shown in Fig. SM1. Interesting to note that, large relative changes (up to 100%) of the surface J_{O1D} exist in high latitudes of NH in the LGM, because of small climatological values there (See Fig. 13a). The cloud fraction decreases in the high latitudes of the NH (Fig. SM2) may also make some contributions to the large increase of surface J_{O1D} there in the LGM, in addition to the total ozone column change (Fig. 11b). On the other hand, an increase in clouds in the midlatitudes (Fig. SM2), especially in the SH, leads to a decrease in J_{O1D} there, partly compensating the effect of total ozone column change.

Figure 13 indicates that the ice sheets have a large local impact on surface J_{O1D} change in the LGM. However, in regions not impacted by ice sheets (e.g., the tropics), the overhead ozone column abundance dominates the LGM change in J_{O1D} , resulting in decreases in photolysis rates in the tropics but increases in most other areas, as compared with the PI.

4. Conclusion and Discussion

We have investigated stratospheric ozone in the LGM using WACCM6. It is shown that, compared to the PI, water vapor in the LGM decreases throughout the stratosphere, with a ~10-25% decrease in the lower and middle stratosphere, and a 20% decrease in the upper stratosphere. This is largely owing to the much lower atmospheric CH₄ concentration, colder CPT (~1.5 K in the tropics) and less water vapor (~1 ppmv) at the CPT. In line with the lower stratospheric water vapor and N₂O concentrations in the LGM, stratospheric OH and NO_x are both decreased by 10-20%, which acts to decrease stratospheric ozone loss rates. On the other hand, because of the lower greenhouse gas concentrations, the stratospheric temperature increases by up to 8 K in the LGM. This results in an increase in the ozone loss rate linked to temperature-sensitive gas-phase reactions, especially a faster Chapman reaction $O + O_3 \rightarrow 2O_2$ [Jonsson et al., 2004]. The net result of these compensating effects is a 5-10% (1-3 DU) decrease in the upper stratospheric ozone concentration, generally consistent with previous studies [Crutzen and Brühl, 1993; Martinerie et al., 1995].

The BDC plays a significant role in determining the spatial distribution of ozone in the lower stratosphere. Contrary to Rind et al. [2001] and Rind et al. [2009], who found a stronger BDC in the lowermost stratosphere in the LGM, Fu et al., [2020] showed that the BDC in the LGM is slower than the modern climate throughout the stratosphere. Because of the weakening of the BDC in the LGM, lower stratospheric ozone increases by 2-5 DU in the tropics and decreases by 5-10 DU in the extratropics. We also examined the effect of lower tropopause in the LGM, which increases the lower-stratospheric ozone in the extratropics and partly compensates the ozone decrease there due to the BDC changes.

In our simulations, we found that tropospheric ozone decreases by about 5 DU (30%) in the LGM, as compared with the PI. Such a result is consistent with theoretical expectation based

on temperature-dependent surface emissions of ozone precursor gases. As shown in Murray et al. [2014], transport of ozone from the stratosphere becomes an increasingly important fraction of the total tropospheric ozone in the cold climate, compared to the modern climate. Hence, changes in stratosphere-troposphere ozone exchange may play an important role in tropospheric chemistry in the LGM. The relative contributions of ozone formed *in situ* in the troposphere versus transport from the stratosphere in the LGM, and its implications for tropospheric chemistry, will be examined in a follow up paper.

It is interesting to note that stratospheric ozone increases significantly in the northeast of North America in the LGM, which is attributed to the local intensification of BDC induced by the Laurentide ice sheet. Compared to PI, the total ozone column in the LGM decreases everywhere, except over the northeast of North America, equatorial Indian and west Pacific Oceans, and East Antarctica, because of the larger stratospheric ozone increases relative to tropospheric ozone decreases there.

Compared to PI, surface J_{O1D} in the LGM increases almost everywhere due to the decreased ozone column abundance. The largest increases are over North America and Europe because of the increase of surface albedo and smaller solar attenuation resulting from the large ice sheets. The large increase of surface J_{O1D} over the SH near 60° S is caused by the increased sea ice extent in the LGM. Surface J_{O1D} decreases in the tropics and the Antarctic in the LGM are due to the increases in the overhead ozone column abundance there. Such UV radiation change may have important ramifications for tropospheric chemistry [e.g. Murray et al., 2014], with potential implications for the methane lifetime as well as for interpretation of some paleoclimate records such as pollen [Benca et al., 2018]. A dynamically consistent ozone field in the LGM can also be expected to be important for model simulations of the LGM climate [e.g. Nowack et al. 2015;

Chiodo and Polvani, 2017; Noda et al., 2017; Szopa et al. 2019]. Therefore, in addition to the implications for tropospheric chemistry, the ozone fields from this study are useful for the PMIP LGM climate simulations.

Acknowledgements: This research was supported by NSF Grant AGS-1821437 and NASA Grant 80NSSC18K1031. SS was supported by NSF AGS project 1848863. RHW was partially funded by the European Union's Horizon 2020 research and innovation programme under the Marie Skłodowska-Curie Grant Agreement No. 797961. We would like to acknowledge high-performance computing support from Cheyenne (doi:10.5065/D6RX99HX) provided by NCAR's Computational and Information Systems Laboratory, sponsored by the National Science Foundation, for the WACCM6 simulations and analyses presented in this study and for the data management, storage and preservation. We intend to provide access to the data by acceptance. The National Center for Atmospheric Research is sponsored by the United States National Science Foundation.

References

- Abe-Ouchi, A., et al. (2015), Ice-sheet configuration in the CMIP5/PMIP3 Last Glacial Maximum experiments, *Geosci Model Dev*, 8(11), 3621-3637, doi:10.5194/gmd-8-3621-2015.
- Andrews, D. G., C. B. Leovy, and J. R. Holton (1987), *Middle atmosphere dynamics*, Academic press.
- Benca, J., I. A. P. Duijnste, and C. V. Looy, (2018), UV-B induced forest sterility: Implications of ozone shield failure in Earth's largest extinction, *Sci. Adv.*, 4(2), e1700618.
- Braconnot, P., S. P. Harrison, M. Kageyama, P. J. Bartlein, V. Masson-Delmotte, A. Abe-Ouchi, B. Otto-Bliesner, and Y. Zhao (2012), Evaluation of climate models using palaeoclimatic data, *Nat Clim Change*, 2(6), 417-424, doi:10.1038/nclimate1456.
- Brady, E. C., B. L. Otto-Bliesner, J. E. Kay, and N. Rosenbloom (2013), Sensitivity to Glacial Forcing in the CCSM4, *J Climate*, 26(6), 1901-1925, doi:10.1175/jcli-d-11-00416.1.
- Brasseur, G. P., and S. Solomon (2006), *Aeronomy of the middle atmosphere: chemistry and physics of the stratosphere and mesosphere*, Springer Science & Business Media.
- Burkholder, J. B., S. P. Sander, J. P. D. Abbatt, J. R. Barker, R. E. Huie, C. E. Kolb, M. J. Kurylo, V. L. Orkin, D. M. Wilmouth, and P. H. Wine (2015), *Chemical kinetics and photochemical data for use in atmospheric studies: Evaluation number 18*, Technical Report, Pasadena, CA : Jet Propulsion Laboratory, National Aeronautics and Space Administration, 2015.
- Chiodo, G., and L. M. Polvani (2017), Reduced Southern Hemispheric circulation response to quadrupled CO₂ due to stratospheric ozone feedback, *Geophys Res Lett*, 44(1), 465-474, doi:10.1002/2016gl071011.
- CLIMAP (1976), The surface of the ice-age earth, *Science*, 1131-1137.

461 Crutzen, P. J., and C. Brühl (1993), A model study of atmospheric temperatures and the
 462 concentrations of ozone, hydroxyl, and some other photochemically active gases during the
 463 glacial, the preindustrial Holocene and the present, *Geophys Res Lett*, 20(11), 1047-1050.
 464 Emmons, L. K., R. H. Schwantes, J. J. Orlando, G. Tyndall, D. Kinnison, J. F. Lamarque, D.
 465 Marsh, M. J. Mills, S. Tilmes, and C. Bardeen (2020), The Chemistry Mechanism in the
 466 Community Earth System Model version 2 (CESM2), *J Adv Model Earth Sy*,
 467 doi:10.1029/2019MS001882.
 468 Fu, Q., C. M. Johanson, J. M. Wallace, and T. Reichler (2006), Enhanced mid-latitude tropospheric
 469 warming in satellite measurements, *Science*, 312(5777), 1179-1179.
 470 Fu, Q., and P. Lin (2011), Poleward Shift of Subtropical Jets Inferred from Satellite-Observed
 471 Lower-Stratospheric Temperatures, *J Climate*, 24(21), 5597-5603, doi:10.1175/jcli-d-11-
 472 00027.1.
 473 Fu, Q., R. H. White, M. Wang, B. Alexander, S. Solomon, A. Gettelman, D. Battisti, and P. Lin
 474 (2020), The Brewer-Dobson Circulation during the Last Glacial Maximum, *Geophys Res Lett*,
 475 doi:10.1029/2019GL086271.
 476 Garcia, R. R., and J. H. Richter (2019), On the Momentum Budget of the Quasi-Biennial
 477 Oscillation in the Whole Atmosphere Community Climate Model, *J Atmos Sci*, 76(1), 69-87,
 478 doi:10.1175/jas-d-18-0088.1.
 479 Geng, L., L. T. Murray, L. J. Mickley, P. Lin, Q. Fu, A. J. Schauer, and B. Alexander (2017),
 480 Isotopic evidence of multiple controls on atmospheric oxidants over climate transitions,
 481 *Nature*, 546(7656), 133-+, doi:10.1038/nature22340.
 482 Gettelman, A., M. Mills, D. Kinnison, R. Garcia, A. Smith, D. Marsh, S. Tilmes, F. Vitt, C.
 483 Bardeen, and J. McInerney (2019), The Whole Atmosphere Community Climate Model

Version 6 (WACCM6), Journal of Geophysical Research: Atmospheres.

Guenther, A., X. Jiang, C. Heald, T. Sakulyanontvittaya, T. Duhl, L. Emmons, and X. Wang (2012), The Model of Emissions of Gases and Aerosols from Nature version 2.1 (MEGAN2.1): an extended and updated framework for modeling biogenic emissions, *Geosci Model Dev*, 5(6), 1471-1492.

Jonsson, A. I., J. de Grandpre, V. I. Fomichev, J. C. McConnell, and S. R. Beagley (2004), Doubled CO₂-induced cooling in the middle atmosphere: Photochemical analysis of the ozone radiative feedback, *J Geophys Res-Atmos*, 109(D24), doi:10.1029/2004jd005093.

Kaplan, J. O., G. Folberth, and D. A. Hauglustaine (2006), Role of methane and biogenic volatile organic compound sources in late glacial and Holocene fluctuations of atmospheric methane concentrations, *Global Biogeochem Cy*, 20(2), doi:10.1029/2005gb002590.

Kucera, M., A. Rosell-Mele, R. Schneider, C. Waelbroeck, and M. Weinelt (2005), Multiproxy approach for the reconstruction of the glacial ocean surface (MARGO), *Quaternary Sci Rev*, 24(7-9), 813-819, doi:10.1016/j.quascirev.2004.07.017.

Lamy, K., et al. (2019), Clear-sky ultraviolet radiation modelling using output from the Chemistry Climate Model Initiative, *Atmos Chem Phys*, 19(15), 10087-10110, doi:10.5194/acp-19-10087-2019.

Lelieveld, J., and F. J. Dentener (2000), What controls tropospheric ozone?, *J Geophys Res-Atmos*, 105(D3), 3531-3551, doi:10.1029/1999jd901011.

LeTexier, H., S. Solomon, and R. R. Garcia (1988), The Role of Molecular Hydrogen and Methane Oxidation in the Water Vapour Budget of the Stratosphere, *Q J Roy Meteor Soc*, 114(480), 281-295, doi:10.1002/qj.49711448002.

Levine, J. G., E. W. Wolff, A. E. Jones, and L. C. Sime (2011), The role of atomic chlorine in

glacial-interglacial changes in the carbon-13 content of atmospheric methane, *Geophys Res Lett*, 38, doi:10.1029/2010gl046122.

Li, F., R. S. Stolarski, and P. A. Newman (2009), Stratospheric ozone in the post-CFC era, *Atmos Chem Phys*, 9(6), 2207-2213, doi:10.5194/acp-9-2207-2009.

Logan, J. A. (1985), Tropospheric ozone: Seasonal behavior, trends, and anthropogenic influence, *J Geophys Res-Atmos*, 90(ND6), 10463-10482, doi:10.1029/JD090iD06p10463.

Martinerie, P., G. P. Brasseur, and C. Granier (1995), The Chemical Composition of Ancient Atmospheres: A Model Study Constrained by Ice Core Data, *J Geophys Res-Atmos*, 100(D7), 14291-14304, doi:10.1029/95jd00826.

McLinden, C. A., S. C. Olsen, B. Hannegan, O. Wild, M. J. Prather, and J. Sundet (2000), Stratospheric ozone in 3-D models: A simple chemistry and the cross-tropopause flux, *J Geophys Res-Atmos*, 105(D11), 14653-14665, doi:10.1029/2000jd900124.

Murray, L. T., L. J. Mickley, J. O. Kaplan, E. D. Sofen, M. Pfeiffer, and B. Alexander (2014), Factors controlling variability in the oxidative capacity of the troposphere since the Last Glacial Maximum, *Atmos Chem Phys*, 14(7), 3589-3622, doi:10.5194/acp-14-3589-2014.

Noda, S., K. Kodera, Y. Adachi, M. Deushi, A. Kitoh, R. Mizuta, S. Murakami, K. Yoshida, and S. Yoden (2017), Impact of interactive chemistry of stratospheric ozone on Southern Hemisphere paleoclimate simulation, *Journal of Geophysical Research: Atmospheres*, 122(2), 878-895.

Nowack, P. J., N. L. Abraham, A. C. Maycock, P. Braesicke, J. M. Gregory, M. M. Joshi, A. Osprey, and J. A. Pyle (2015), A large ozone-circulation feedback and its implications for global warming assessments, *Nat Clim Change*, 5(1), 41-45, doi:10.1038/nclimate2451.

Oleson, K. W., D. M. Lawrence, B. Gordon, M. G. Flanner, E. Kluzek, J. Peter, S. Levis, S. C.

Swenson, E. Thornton, and J. Feddema (2010), Technical description of version 4.0 of the Community Land Model (CLM).

Pan, L. L., S. B. Honomichl, T. V. Bui, T. Thornberry, A. Rollins, E. Hintsa, and E. J. Jensen (2018), Lapse Rate or Cold Point: The Tropical Tropopause Identified by In Situ Trace Gas Measurements, *Geophys Res Lett*, 45(19), 10,756-710,763.

Price, C., and D. Rind (1992), A Simple Lightning Parameterization for Calculating Global Lightning Distributions, *J Geophys Res-Atmos*, 97(D9), 9919-9933, doi:10.1029/92jd00719.

Randel, W. J., F. Wu, S. J. Oltmans, K. Rosenlof, and G. E. Nedoluha (2004), Interannual changes of stratospheric water vapor and correlations with tropical tropopause temperatures, *J Atmos Sci*, 61(17), 2133-2148, doi:10.1175/1520-0469(2004)061<2133:Icoswv>2.0.Co;2.

Rayner, N. A., D. E. Parker, E. B. Horton, C. K. Folland, L. V. Alexander, D. P. Rowell, E. C. Kent, and A. Kaplan (2003), Global analyses of sea surface temperature, sea ice, and night marine air temperature since the late nineteenth century, *J Geophys Res-Atmos*, 108(D14), doi:10.1029/2002jd002670.

Rind, D., M. Chandler, P. Lonergan, and J. Lerner (2001), Climate change and the middle atmosphere 5. Paleostratosphere in cold and warm climates, *J Geophys Res-Atmos*, 106(D17), 20195-20212, doi:10.1029/2000jd900548.

Rind, D., J. Lerner, C. McLinden, and J. Perlwitz (2009), Stratospheric ozone during the Last Glacial Maximum, *Geophys Res Lett*, 36, doi:10.1029/2009gl037617.

Rohrer, F., and H. Berresheim (2006), Strong correlation between levels of tropospheric hydroxyl radicals and solar ultraviolet radiation, *Nature*, 442(7099), 184-187, doi:10.1038/nature04924.

Rosenlof, K. H. (1995), Seasonal cycle of the residual mean meridional circulation in the stratosphere, *J Geophys Res-Atmos*, 100(D3), 5173-5191, doi:10.1029/94jd03122.

Solomon, S., D. Kinnison, J. Bandoro, and R. Garcia (2015), Simulation of polar ozone depletion:
 An update, *J Geophys Res-Atmos*, 120(15), 7958-7974, doi:10.1002/2015jd023365.

Szopa, S., R. Thieblemont, S. Bekki, S. Botsyun, and P. Sepulchre (2019), Role of the stratospheric
 chemistry-climate interactions in the hot climate conditions of the Eocene, *Clim Past*, 15(4),
 1187-1203, doi:10.5194/cp-15-1187-2019.

Thornton, P. E., J. F. Lamarque, N. A. Rosenbloom, and N. M. Mahowald (2007), Influence of
 carbon-nitrogen cycle coupling on land model response to CO₂ fertilization and climate
 variability, *Global Biogeochem Cy*, 21(4), doi:10.1029/2006GB002868.

Valdes, P. J., D. J. Beerling, and C. E. Johnson (2005), The ice age methane budget, *Geophys Res*
Lett, 32(2), doi:10.1029/2004gl021004.

Wegner, T., D. E. Kinnison, R. R. Garcia, and S. Solomon (2013), Simulation of polar
 stratospheric clouds in the specified dynamics version of the whole atmosphere community
 climate model, *J Geophys Res-Atmos*, 118(10), 4991-5002, doi:10.1002/jgrd.50415.

World Meteorological Organization (1957). Meteorology—A three dimensional science: Second
 session of the Commission for Aerology. *WMO Bulletin*, IV(4), 134–138.

576 Figure captions

577 Figure 1. Annual-mean zonal-mean temperature change (color scale) for LGM_{PMIP3} versus PI.

578 Black contours show the annual-mean climatology (K) of PI.

579 Figure 2. Annual-mean zonal-mean a) cold point tropopause (CPT) temperature and c) water vapor

580 (H₂O) concentration at the CPT in 3 simulations. Panels b) and d) are the changes of CPT

581 temperature and H₂O concentration at the CPT relative to PI.

582 Figure 3. Annual-mean percentage changes of a) water vapor (H₂O), b) hydroxyl radical (OH),

583 and c) nitrogen oxides (NO_x) for LGM_{PMIP3} versus PI. Black contours show the climatology of

584 PI expressed in a) ppmv, b) pptv and c) ppbv, respectively.

585 Figure 4. Annual-mean percentage change of ozone (color scale) for LGM_{PMIP3} versus PI. Black

586 contours show the climatology (ppmv) of PI.

587 Figure 5. Advective ozone transport (far-left), and its vertical (middle) and meridional (far-right)

588 components in the climatology of PI (upper panels) as well as the changes in LGM_{PMIP3} versus

589 PI (lower panels).

590 Figure 6. Annual-mean zonal-mean column ozone concentrations for various atmospheric layers

591 (upper panels) and the changes relative to PI (lower panels).

592 Figure 7. Spatial distribution of stratospheric ozone column in a) PI simulation, and b) the absolute

593 change for LGM_{PMIP3} versus PI.

594 Figure 8. Spatial distribution of lapse-rate tropopause (LRT) pressure change for LGM_{PMIP3} versus

595 PI.

596 Figure 9. Spatial distribution of ozone column changes in the a) upper and b) lower stratosphere

597 between LGM_{PMIP3} and PI. Panels c) and d) are the lower stratospheric ozone column changes

598 resulting from the tropopause and transport changes.

Figure 10. Same as Figure 7, but for tropospheric ozone column.

Figure 11. Same as Figure 7, but for total ozone column.

Figure 12. Annual-mean absolute change in photolysis rate constant (J_{O1D}) for the reaction $O_3 + hv \rightarrow O_2 + O(^1D)$ in LGM_{PMIP3} versus PI. Black contours show the climatology (day^{-1}) of PI.

Figure 13. Spatiotemporal distribution of surface photolysis rate J_{O1D} in a) PI simulation, and b) the absolute change for LGM_{PMIP3} versus PI. Each row contains two plots sharing a common ordinate axis (latitude). From left to right, a Hovmöller diagram presents the seasonality of zonal mean surface photolysis rate, and a map presents the horizontal distribution.

622 Table 1. Model Simulations.

Simulation names	LGM _{PMIP3}	LGM _{PROXY}	PI
CO ₂	185 ppm	185 ppm	284 ppm
CH ₄	349 ppb	349 ppb	810 ppb
N ₂ O	200 ppb	200 ppb	273 ppb
ODS	0	0	0
CO	Fires	0.1 × Preind.	Year 1850
	Ocean	Preind.	Year 1850
	Fuel Combustion	0	Year 1850
NO _x	Lighting	Interactive	Interactive
	Fires	0.1 × Preind.	Year 1850
	Soil	0.98 × Preind.	Year 1850
	Fuel Combustion	0	Year 1850
SSTs	PMIP3* multi-model mean	MARGO proxy data	1870-1890 average
Sea ice	PMIP3 multi-model mean	PMIP3 multi-model mean	1870-1890 average
Ice sheet topography	Abe-Ouchi et al. [2015]	Abe-Ouchi et al. [2015]	Modern climate
Orbital forcing	21,000 years ago	21,000 years ago	Year 1850

* PMIP3 is Paleoclimate Modeling Intercomparison Project Phase 3.

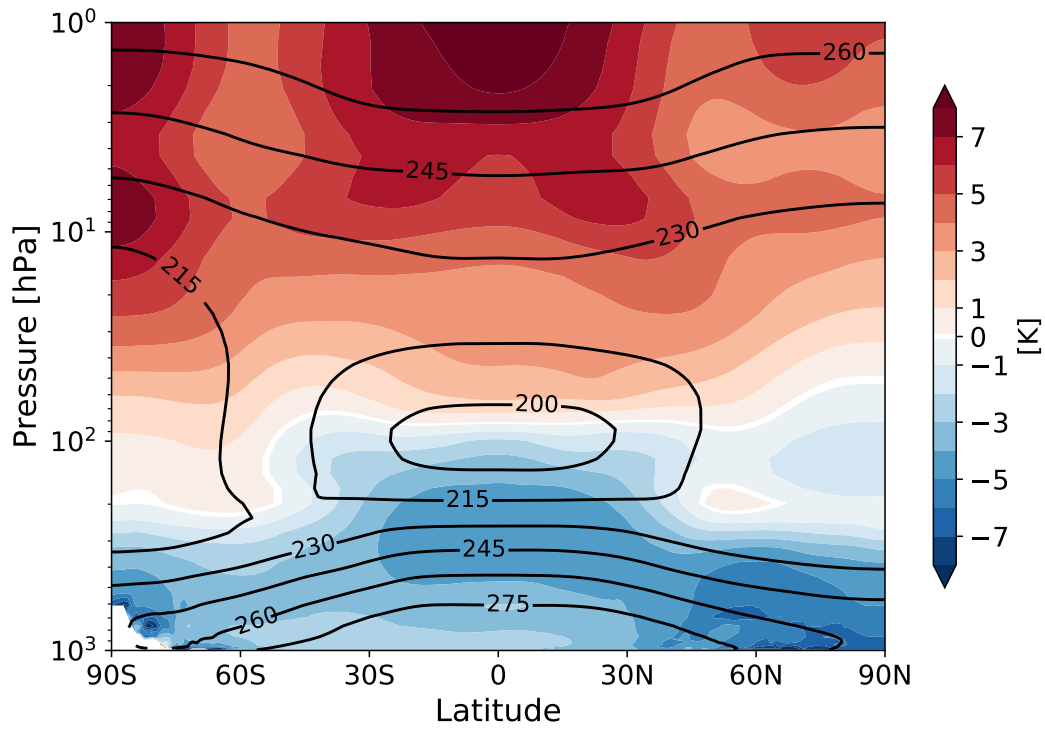


Figure 1. Annual-mean zonal-mean temperature change (color scale) for LGM_{PMIP3} versus PI. Black contours show the annual-mean climatology (K) of PI.

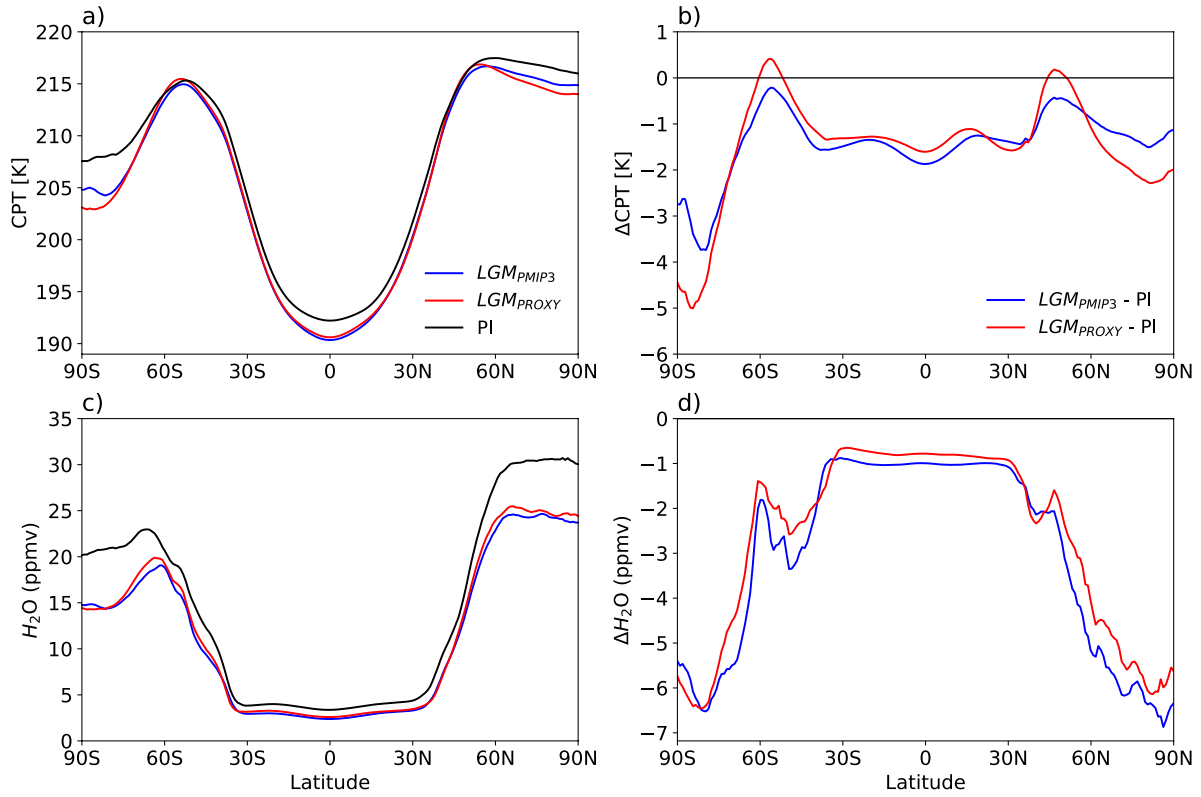


Figure 2. Annual-mean zonal-mean a) cold point tropopause (CPT) temperature and c) water vapor (H_2O) concentration at the CPT in 3 simulations. Panels b) and d) are the changes of CPT temperature and H_2O concentration at the CPT relative to PI.

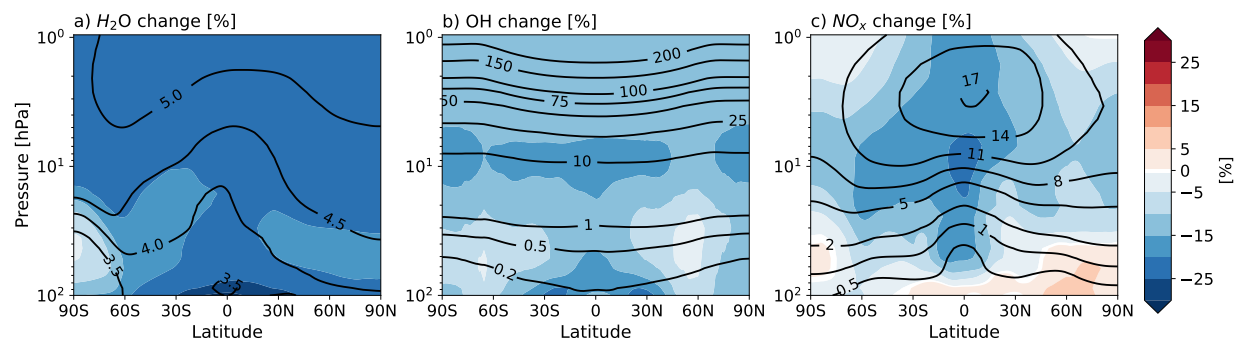


Figure 3. Annual-mean percentage changes of a) water vapor (H_2O), b) hydroxyl radical (OH), and c) nitrogen oxides (NO_x) for LGM_{PMIP3} versus PI . Black contours show the climatology of PI expressed in a) ppmv, b) pptv and c) ppbv, respectively.

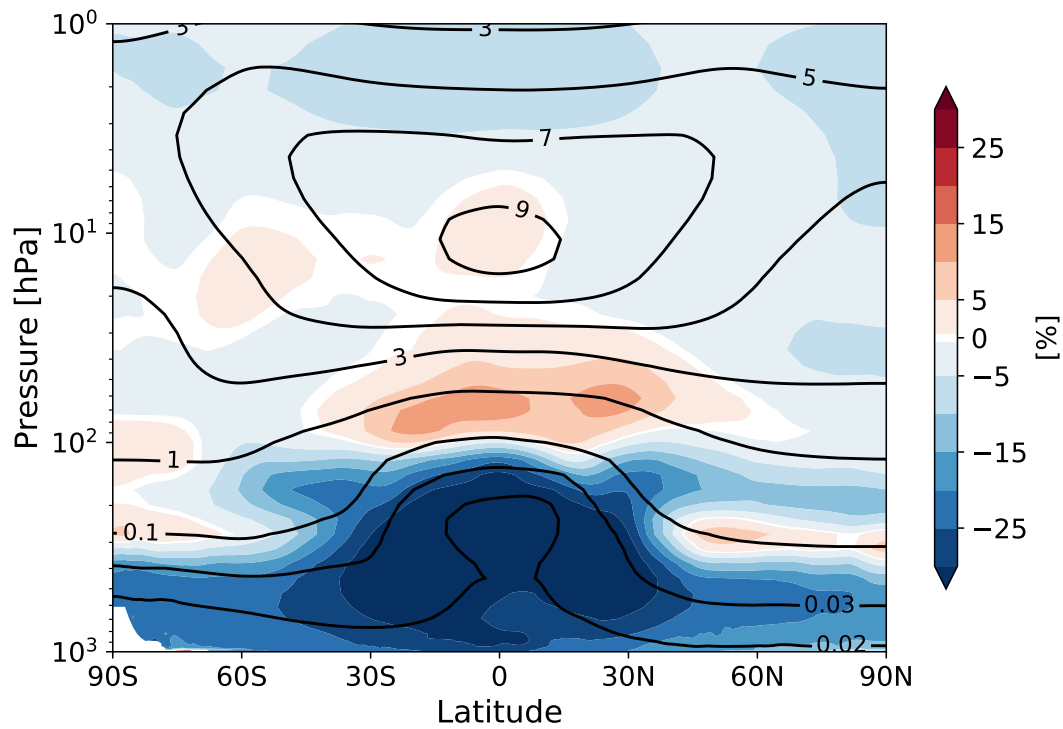


Figure 4. Annual-mean percentage change of ozone (color scale) for LGM_{PMIP3} versus PI. Black contours show the climatology (ppmv) of PI.

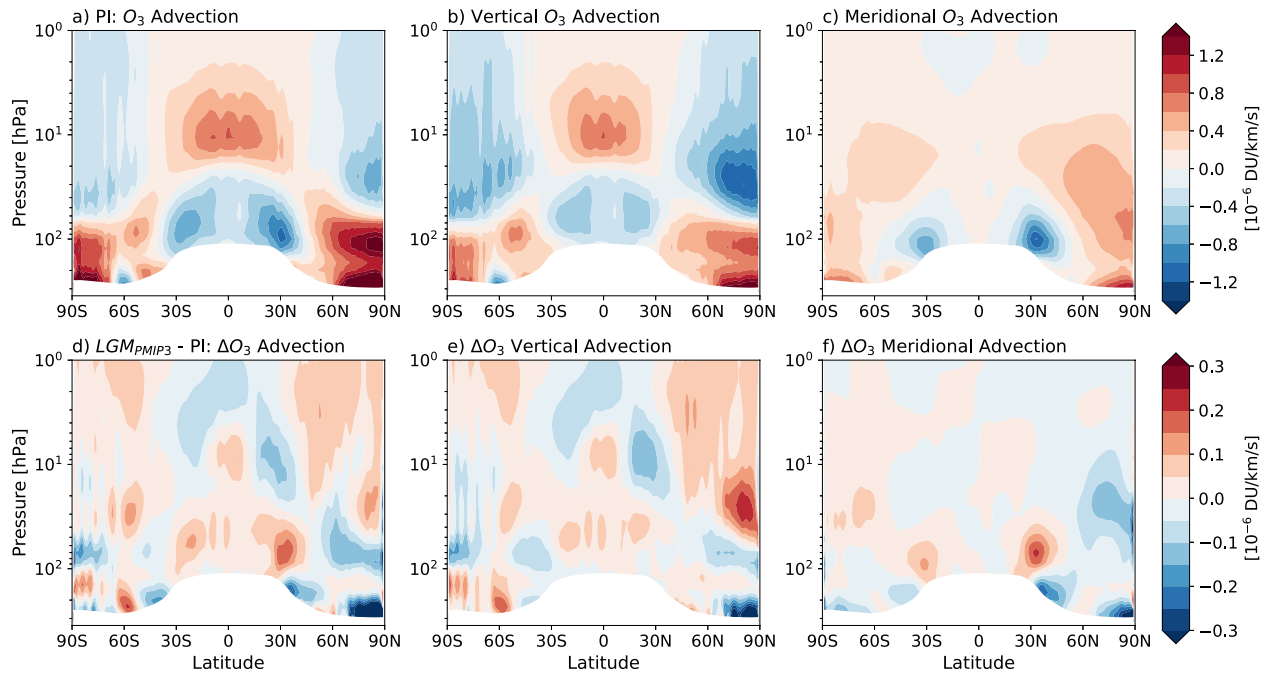


Figure 5. Advective ozone transport (far-left), and its vertical (middle) and meridional (far-right) components in the climatology of PI (upper panels) as well as the changes in LGM_{PMIP3} versus PI (lower panels).

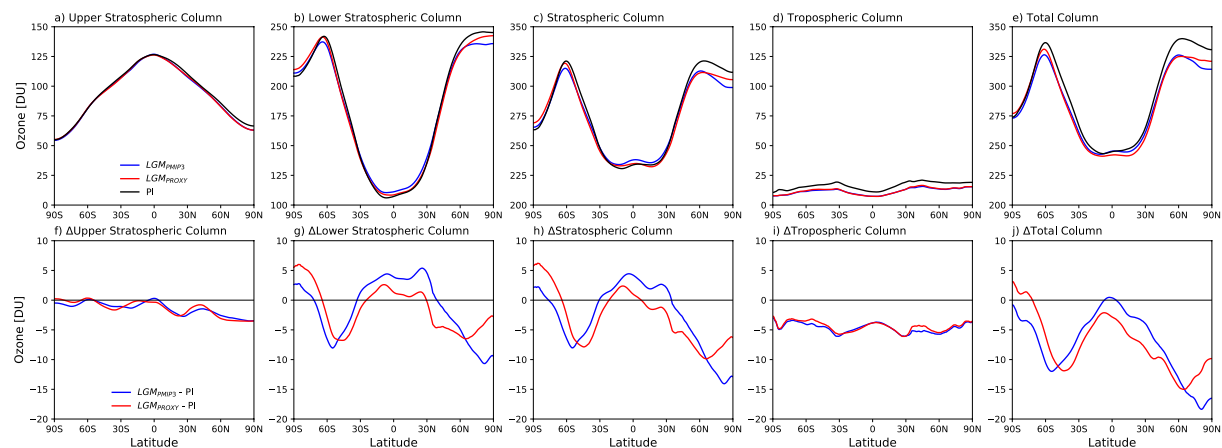


Figure 6. Annual-mean zonal-mean column ozone concentrations for various atmospheric layers (upper panels) and the changes relative to PI (lower panels).

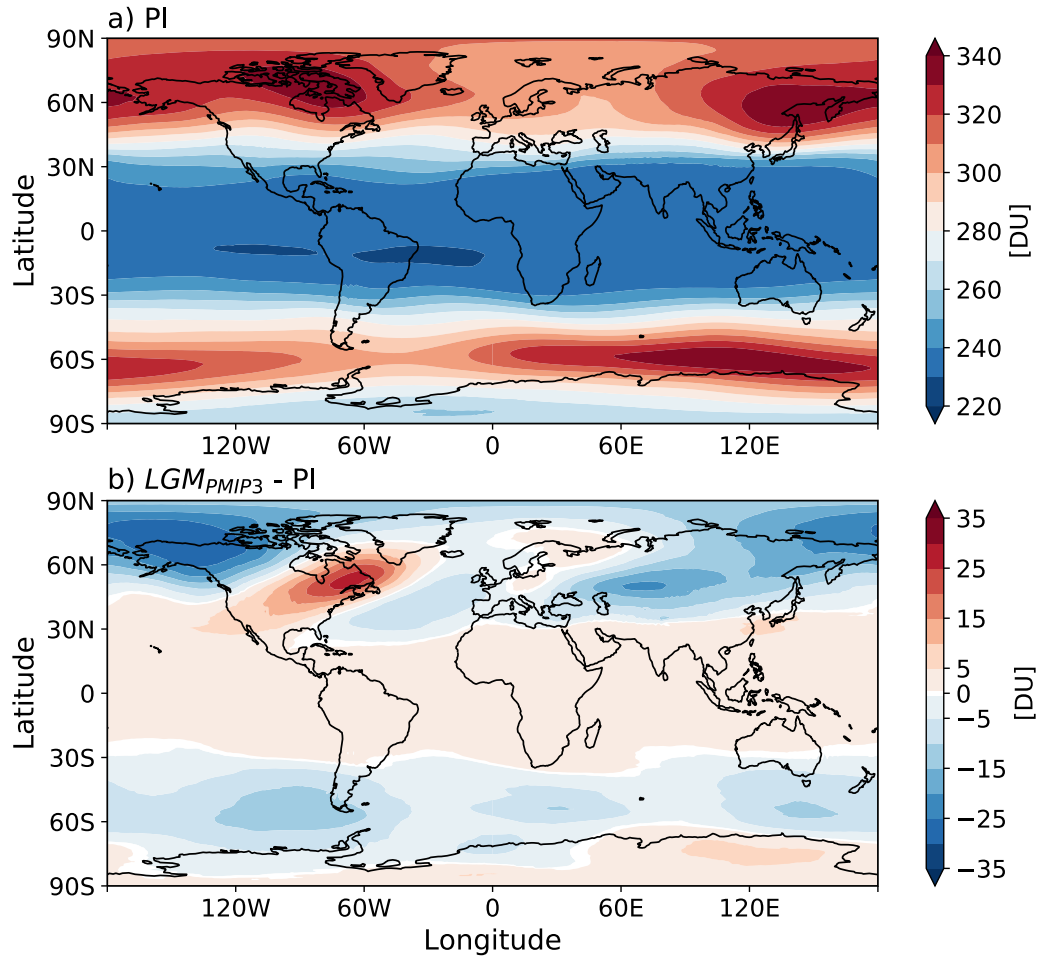


Figure 7. Spatial distribution of stratospheric ozone column in a) PI simulation, and b) the absolute change for LGM_{PMIP3} versus PI.

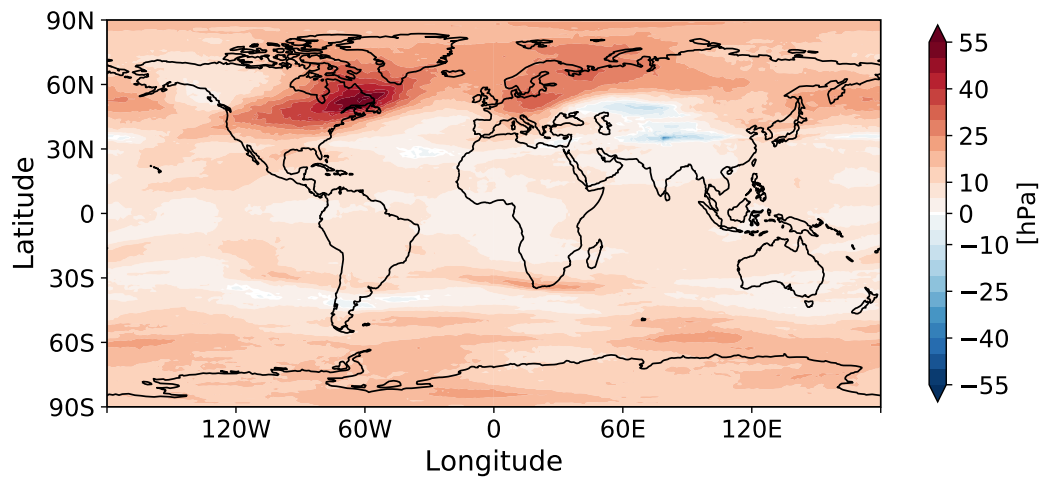


Figure 8. Spatial distribution of lapse-rate tropopause (LRT) pressure change for LGM_{PMI3} versus PI.

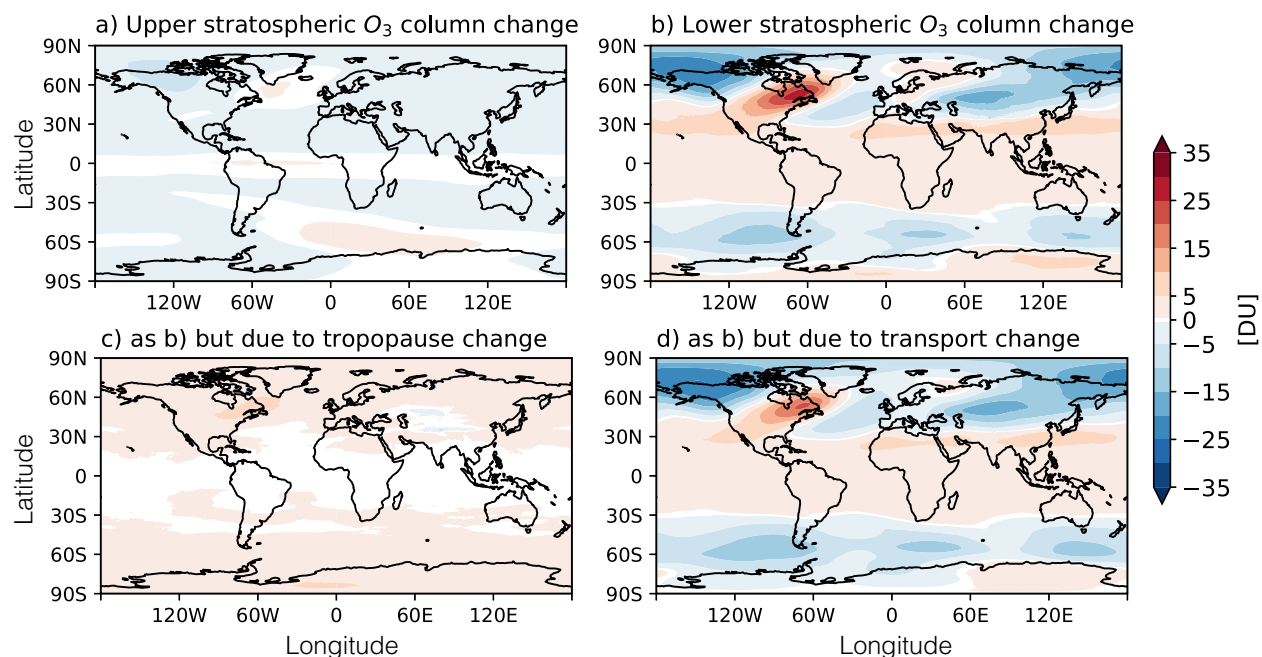


Figure 9. Spatial distribution of ozone column changes in the a) upper and b) lower stratosphere between LGM_{PMIP3} and PI. Panels c) and d) are the lower stratospheric ozone column changes resulting from the tropopause and transport changes.

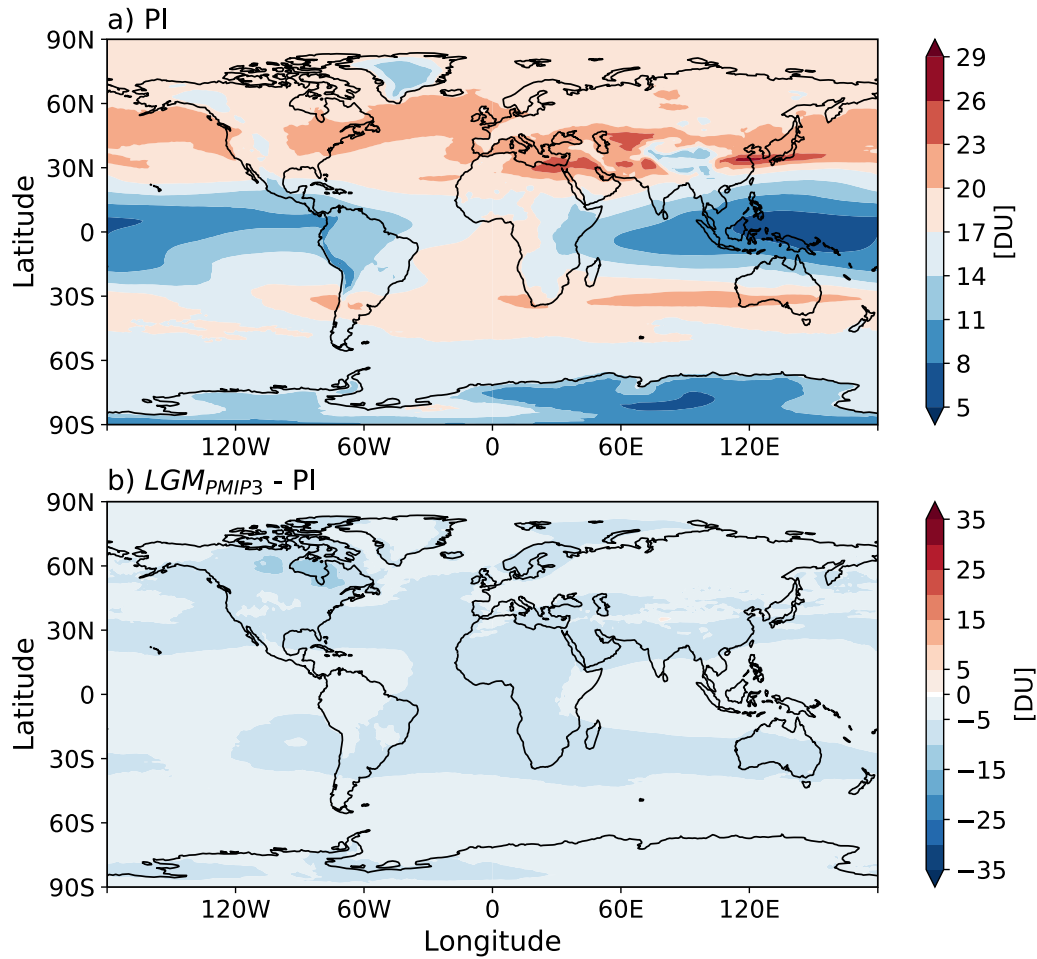


Figure 10. Same as Figure 7, but for tropospheric ozone column.

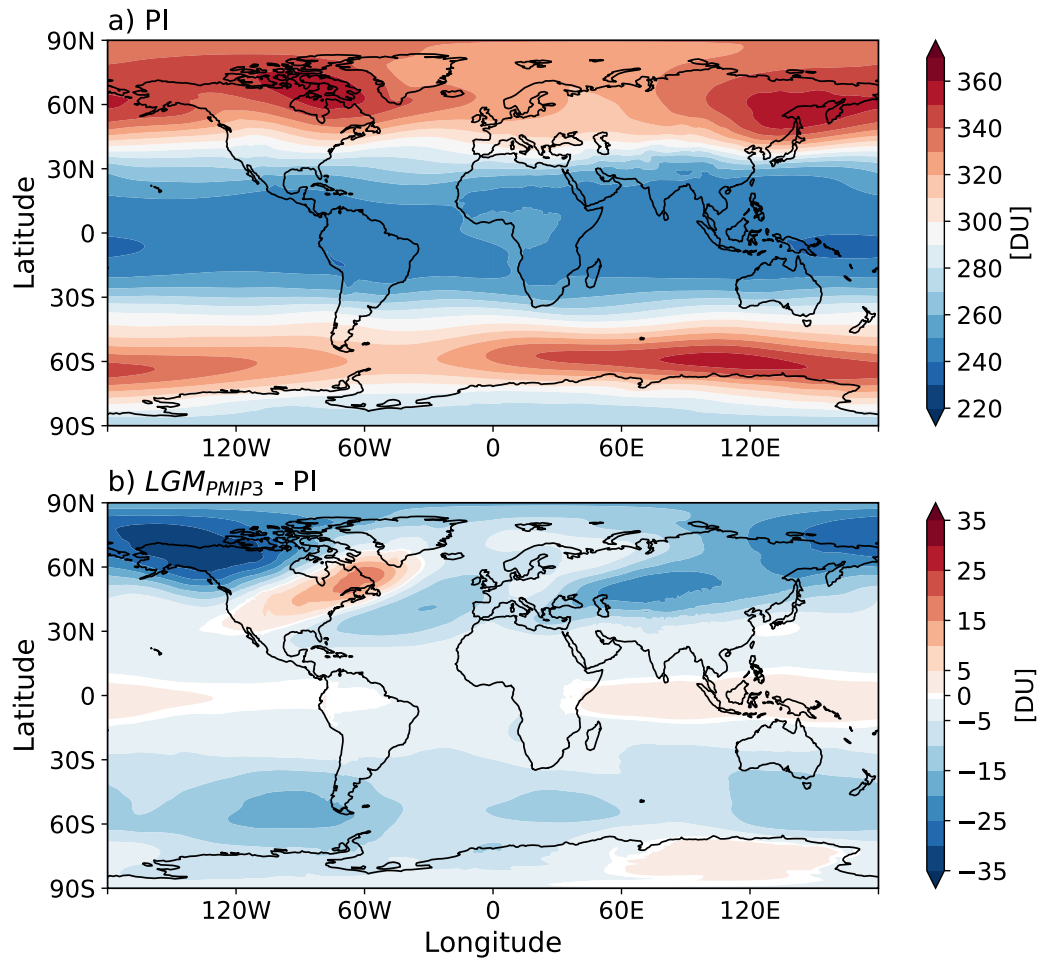


Figure 11. Same as Figure 7, but for total ozone column.

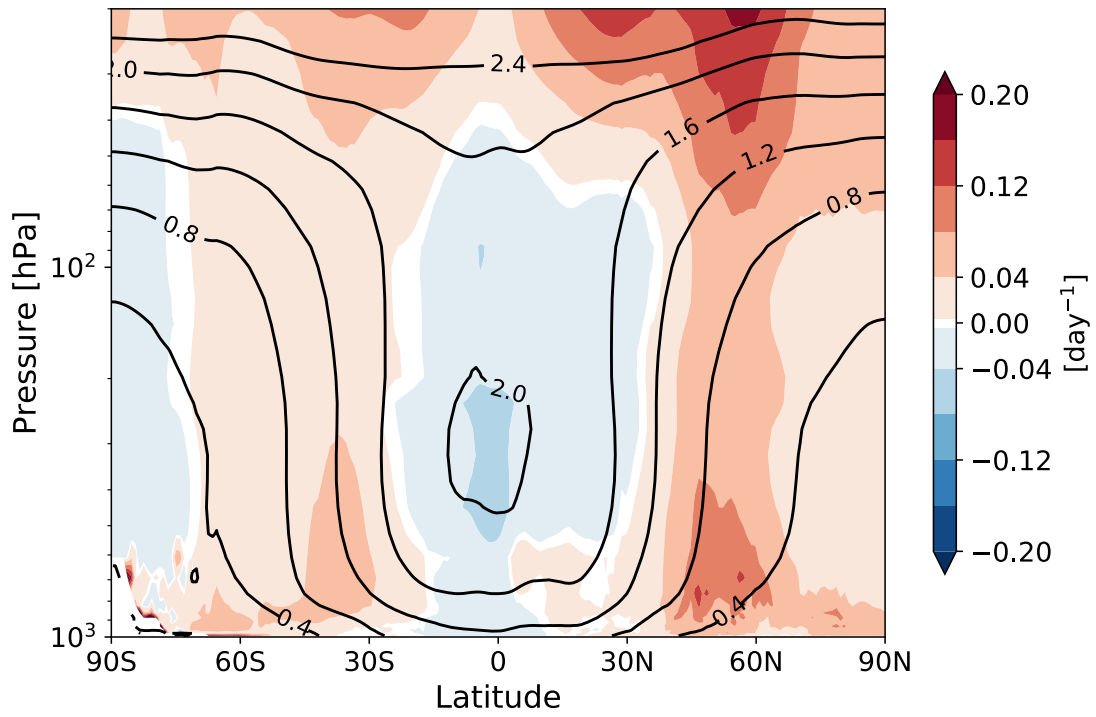


Figure 12. Annual-mean absolute change in photolysis rate constant ($J_{O(1D)}$) for the reaction $O_3 + h\nu \rightarrow O_2 + O(^1D)$ in LGM_{PMIP3} versus PI. Black contours show the climatology (day^{-1}) of PI.

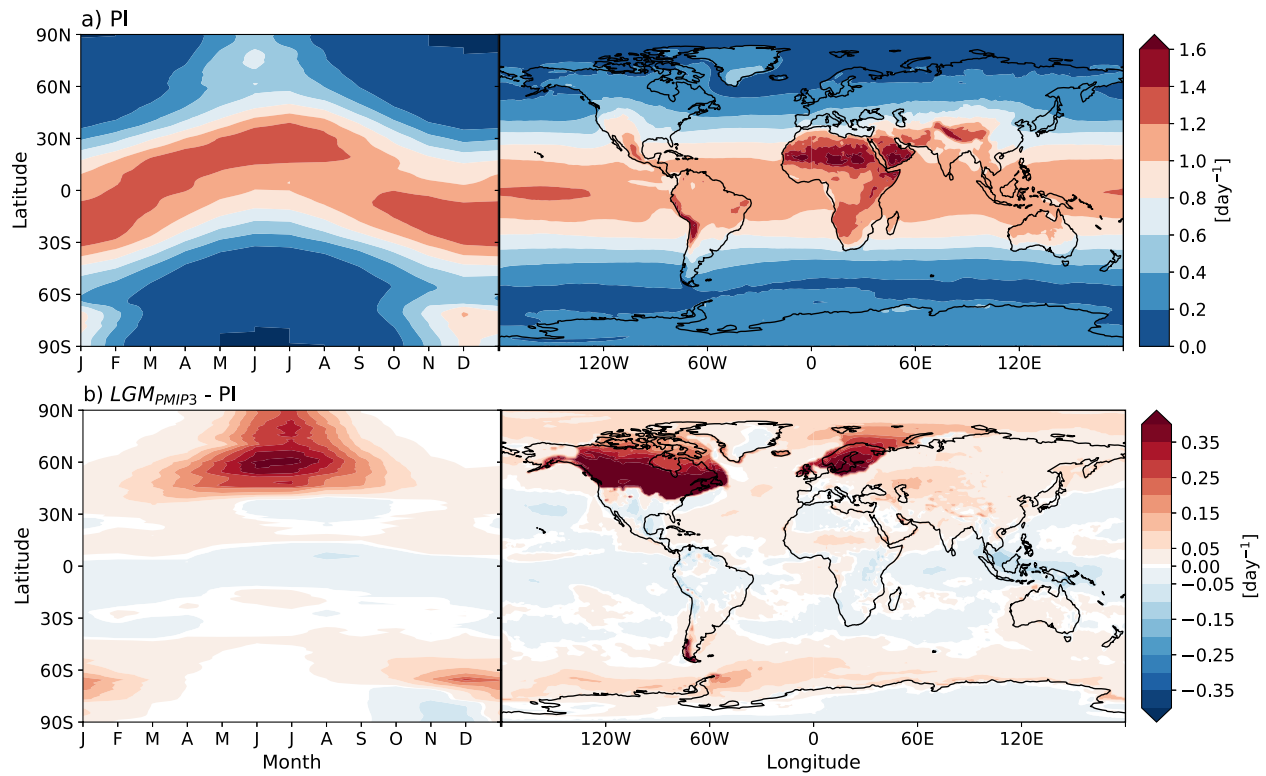


Figure 13. Spatiotemporal distribution of surface photolysis rate J_{O1D} in a) PI simulation, and b) the absolute change for LGM_{PMI3} versus PI. Each row contains two plots sharing a common ordinate axis (latitude). From left to right, a Hovmöller diagram presents the seasonality of zonal mean surface photolysis rate, and a map presents the horizontal distribution.